Nature of interfacial Dzyaloshinskii-Moriya interactions in graphene/Co/Pt(111) multilayer heterostructures

M. Blanco-Rey [1,2] G. Bihlmayer [3] A. Arnau [1,4,2] and J. I. Cerdá[5,*]

[1]*Departamento de Polímeros y Materiales Avanzados: Física, Química y Tecnología, Universidad del País Vasco UPV/EHU, Apartado 1072, 20080 Donostia-San Sebastián, Spain*

[2]*Donostia International Physics Center, Paseo Manuel de Lardizábal 4, 20018 Donostia-San Sebastián, Spain*

[3]*Peter Grünberg Institut and Institute for Advanced Simulation, Forschungszentrum Jülich and JARA, 52425 Jülich, Germany*

[4]*Centro de Física de Materiales CFM/MPC (CSIC-UPV/EHU), Paseo Manuel de Lardizábal 5, 20018 Donostia-San Sebastián, Spain*

[5]*Instituto de Ciencia de Materiales de Madrid, CSIC, Cantoblanco, 28049 Madrid, Spain*

Density-functional theory calculations utilizing the generalized Bloch theorem show that interfacial Dzyaloshinskii-Moriya interactions (DMI) at both interfaces of graphene/Co_n/Pt(111) multilayer heterostructures are decoupled for $n \geqslant 3$. Unlike the property of magnetocrystalline anisotropy, DMI in this system is not strongly affected by stacking defects in the Co layer. The effect of graphene (Gr) is to invert the chirality of the vaccum/Co interfacial DMI, overall reducing the DMI of the heterostructure, which is nevertheless dominated by the strong spin-orbit coupling (SOC) of Pt. A spectral analysis in reciprocal space shows that DMI at both the Gr/Co and Co/Pt interfaces have similar contributions from the strongly hybridized SOC-split d bands. Our analysis proves that the DMI in this family of Gr-capped $3d/5d$ metal heterostructures displays richer physics than what is expected from the prediction of single-band models, such as the Rashba DMI model.

I. INTRODUCTION

When the magnetic exchange interactions are subject to sufficiently intense spin-orbit coupling (SOC) in an environment with broken inversion symmetry, an antisymmetric term appears that leads to a canted and chiral orientation of spins, known as Dzyaloshinskii-Moriya interaction (DMI). First observed for oxides [1] and modeled as orbital-magnetic-moment-dependent terms added to the Anderson Hamiltonian [2,3], it was later reformulated for metallic alloys with diluted magnetic impurities (Fert-Levy model) as a SOC correction to the RKKY exchange [4,5].

Because of the broken inversion symmetry requirement, DMI is usually active at surfaces and interfaces, where it triggers complex chiral ordered spin structures at the nanoscale, such as cycloidal textures [6,7] and skyrmions [8–10], and introduces a unique winding of domain walls [11]. The latter property has been exploited in synthetic magnets [12,13].

Improving the stability of chiral structures, which is lost if symmetric exchange interactions dominate, has been identified as a near-future challenge in the field of magnetic materials [14]. Asymmetric multilayering is used to enhance DMI, since interfaces contribute additively [15–17]. For example, in Ir/Co/Pt- [15] and Pt/Co/Ta-based heterostructures [18] skyrmions of diameter ∼100 nm have been stabilized at room temperature. Contact between a ferromagnet and a heavy nonmagnetic phase is the obvious way to promote DMI, as hybridization with the spin-orbit split $5d$ bands facil-

itates the needed spin-flip electron excitations. Hence Co/Pt has become a paradigmatic system [19–21]. Alternatively, DMI strength and handedness can also be manipulated by adsorption of light element atoms, e.g., hydrogen [22,23] and oxygen [24,25], or capping with graphene (Gr) [23,26] and hexagonal boron nitride [27]. This DMI variation upon adsorption stems from the charge density redistribution at the surface and it is correlated with the electric dipole at the surfaces [24], where the correlation is endorsed by an analytical expression [28]. The prospect of connecting DMI to other, more accessible, properties of the system, such as electrostatic ones, has motivated the search for DMI descriptors that allow its predictability in systems of potential interest. For example, at a $3d/5d$ interface, it correlates with the spin moment m_S of the $3d$ atoms but not with the m_S induced at the interfacial $5d$ atoms [19–21,28,29], neither with the spin dipole nor with the orbital magnetic moments [28]. Direct modification of DMI merely based in electric field manipulation by a STM tip is questionable, as it may be mistaken for a variation of the magnetic exchange coupling strength [30].

In an attempt to classify DMI into types, it has been argued that Co/Pt and Gr/Co interfacial DMI are of different nature, namely Fert-Levy-like and Rashba-like, respectively [31]. In the former interface, the DMI energy contribution localizes at Pt, which has strong atomic SOC strength ξ. In the latter, Gr/Co, the aforementioned induced electrostatic potential change ∇V is modeled by a one-band Rashba Hamiltonian in the presence of a Heisenberg exchange term [32–34], leading to a linear term in the electron wave vector **k**. These models

can be considered as limits of the strongly hybridized SOC-split d-bands behavior.

Motivated by recent experimental work on multilayer Gr/Co$_n$/Pt(111) heterostructures [26,35] and by the existing density-functional theory (DFT) work on the individual interfaces of them, in this paper we show that DMI cannot be satisfactorily described in either limit model. Our DFT calculations reveal that the Pt SOC dominates overall and that there are sizable contributions from Co SOC locally, although cancellations occur for Co from both interfaces. The DMI chirality induced by the graphene capping is opposite to and of the same order of magnitude as that of the Co/Pt interface, in agreement with the observation of Ref. [26]. We draw the important conclusion that this result cannot be simply attributed to specific states in the reciprocal space, i.e., a single-band Rashba model cannot account for it. This finding can be extrapolated to other $2p/3d/5d$ heterostructures, where SOC will split bands that undergo a similar strong hybridization of the $3d$ bands upon interface formation, as it happens in, for example, the cases of Gr/Co/Ir(111) [35] and O/Fe/Ir(100) [24].

During pseudomorphic growth by intercalation in Gr/Pt, Co attains a fcc stacking with interplanar spacing contraction (fcc*). Therefore, the central regions of the slab are locally centrosymmetric and DMI is solely an interfacial effect. In the present work we show that this regime is reached at Co$_3$ thickness and that the DMI contributions of the stacking defects cancel out. Interestingly, this DMI behavior contrasts with that of the magnetocrystalline anisotropy of fcc* Gr/Co$_n$/Pt(111), where a complex evolution as a function of the Co$_n$ thickness is found that depends on the competition between the contributions from the fcc* bulk (in plane) and twin boundary defects (out of plane) [35].

The paper is organized as follows. In Sec. II we describe the model structures of Gr/Co$_n$/Pt used in this work and the details of the DFT calculations based on the generalized Bloch theorem with SOC. The Results and Discussion section is split into a collection of thickness-dependent and layer-resolved DMI energies (Sec. III A), as well as an analysis in the reciprocal space (Sec. III B), where the DMI contributions are energy and wave vector resolved. Finally, conclusions are drawn.

II. THEORETICAL METHODS

The pseudovectors $\mathbf{D}_{ij}$ characterize the DMI between two localized spin moments $\mathbf{S}_i, \mathbf{S}_j$, which is expressed as the Hamiltonian term $\sum_{\langle ij \rangle} \mathbf{D}_{ij} \cdot \mathbf{S}_i \times \mathbf{S}_j$. Figure 1 shows the D vectors between the Co atom at the origin unit cell and its six closest Co atoms in the case of a monolayer. The threefold axes and mirror planes in the structure constrain these D vectors to be determined by two free parameters D_y and D_z [36], as indicated in the sketch. Note that the relative positions of the nearest Pt atom with respect to each pair of Co neighbors alternate from right to left in the threefold symmetry and, thus, the D vector out-of-plane component D_z alternates in sign. As this work is restricted to relatively small angles between spins, we will use an effective model of the energy that maps all Co-Co interactions in the model slabs onto a two-dimensional Hamiltonian that depends on effective D_y and D_z parameters (see Fig. 1 and Supplemental Material
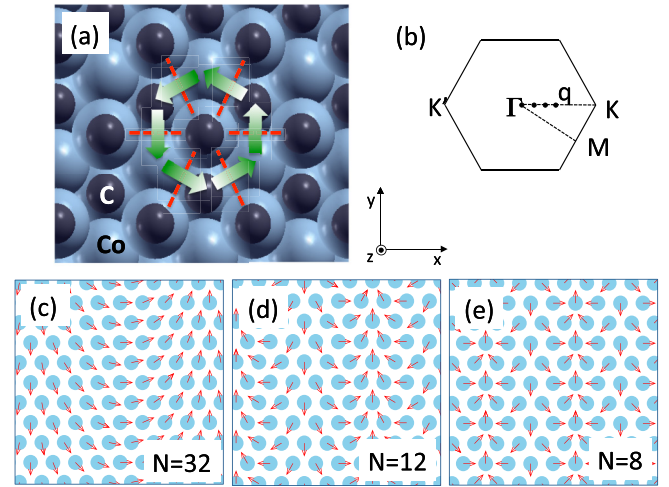

FIG. 1. (a) Top view of a graphene-covered fcc* Co slab. For the topmost Co plane, the central atom D vectors of the DMI with its in-plane nearest neighbors (red dashed segments) are indicated by thick arrows with threefold symmetry. The color gradient from green to white depicts the D_z component sign. (b) The spin spiral wave vectors used in this work belong to the ΓK direction of the Brillouin zone, i.e., $\mathbf{q} = \frac{2\pi}{a}(\frac{1}{N}, \frac{1}{N}, 0)$. (c)–(e) Examples of the spin orientations in a Co plane for three N values.

[37] Fig. S1). Being effective constants, D_y and D_z can be interpreted also as micromagnetic-scale properties and can be used as input for simulations. The DFT values can be used directly in the spin dynamics equations of atomistic simulations (e.g., Refs. [17,38]). Alternatively, different procedures can be applied to transform them into energy densities [19] to be used in continuum modeling (e.g., Refs. [11,39]).

DFT calculations in the full-potential linearized augmented plane waves (FLAPW) formalism [40,41] have been carried out with the FLEUR code [42,43]. The Perdew-Burke-Ernzerhof (PBE) formulation is chosen as the exchange and correlation functional [44] for this work. We have used Co layers of one to five atom thicknesses, pseudomorphic on a fcc Pt(111) substrate (lateral periodicity 2.772 Å) of five atomic planes, with the relaxed interplanar spacings found in Ref. [35]. The effect of the substrate thickness on the DMI is shown in the Supplemental Material Fig. S2. For the basis set, a $48 \times 48 \times 1$ Monkhorst-Pack-point mesh [45] is used and plane wave expansion cutoffs of 4, 11, and 9.5 a.u.$^{-1}$ for the wave functions, density, and potential, respectively. The local basis was constructed without local orbitals, with $l_{max} = 6, 8,$ and 10 for C, Co, and Pt, respectively. The smearing energy for the Fermi level determination was 0.03 eV.

Suitable noncollinear spin structures are needed for the model to show DMI. They are modeled as long-wavelength spin spirals in the generalized Bloch theorem (GBT) approach [46], which imposes a longer periodicity of the magnetization density described by a wave vector $\mathbf{q}$. Although, in principle, the charge density can be self-consistently converged for a given $\mathbf{q}$, since the calculations shown here involve long-wavelength spirals, we use the GBT non-self-consistently to calculate new energies and electron wave functions as a perturbation of a $\mathbf{q} = 0$ ground state (see Supplemental Material

Fig. S3). Our calculations on the minimal model system, a $Gr/Co_1/Pt_1$ trilayer, show that this is a fair approximation in the low-q regime (see Supplemental Material Fig. S4). Finally, spin-orbit interactions are added as a first-order perturbation. The implementation of this procedure in the FLAPW code is described in Ref. [47].

We use flat spin spirals with a spin rotation axis $\hat{s}_a$, which yield a chirality dependent energy in the presence of SOC. The energy difference between axes pointing in opposite directions $\hat{s}_a^+ (\hat{s}_a^-)$ is the DMI energy for a given spiral with **q** periodicity. Our convention is that the spirals are counterclockwise (CCW) with respect to $\hat{s}_a$, so that $\hat{s}_a^+ (\hat{s}_a^-)$ mean CCW (CW) or left-handed (right-handed) spirals. Therefore, if the energy difference $\Delta E_{DMI}^{\hat{s}_a}(\mathbf{q}) = E_{DMI}(\mathbf{q}; \hat{s}_a^+) - E_{DMI}(\mathbf{q}; \hat{s}_a^-)$ is positive (negative), a CW (CCW) spiral is favored. The FLAPW calculations of this work are run for spirals with **q** vectors along the ΓK direction of the two-dimensional first Brillouin zone, i.e., the $\mathbf{q} = \frac{2\pi}{a}(\frac{1}{N}, \frac{1}{N}, 0)$ direction in the Brillouin zone. As an example, Fig. 1 shows the spins of a Co atomic plane in the cases of $N = 32, 12, 8$ and $\hat{s}_a = Z$. We used N values between 8 and 48 (the latter is at the resolution limit set by our electron momentum **k** calculation grid, $48 \times 48 \times 1$).

III. RESULTS AND DISCUSSION

A. Additivity of interfacial DMI

At low q values, the DMI energies for spins rotating around $\hat{s}_a$ pointing in the (positive) Y and Z axes follow a nearly linear in q and a q^3 dependence, respectively, as we describe next. These trends are observed in Fig. 2 (red symbols and lines), which show $\Delta E_{DMI}^{\hat{s}_a}(\mathbf{q})$ for $Gr/Co_n/Pt_5$, $n = 1–5$, slabs in the low-q regime. Nevertheless, for the in-plane spins case the energies are too low to extract accurate quantitative results from a fit (note that the energies are one order of magnitude smaller for these spirals). The evolution of $\Delta E_{DMI}^Y(\mathbf{q})$ with the Co layer thickness (red line) shows a significant magnitude variation, but no chirality change (i.e., no sign change). The D_y effective parameter is extracted from the fit to a 2D model with nearest neighbor interactions in a hexagonal lattice with C_{3v} symmetry, given by the expression (see Fig. S1)

$$\Delta E_{DMI}^{\hat{s}_a}(\mathbf{q})$$
$$= 4S^2 \sin\theta \hat{s}_a \cdot [0, D_y(1 + 2\cos\theta), 2D_z(\cos\theta - 1)] \quad (1)$$

for flat spin spirals $\mathbf{q} = \frac{2\pi}{a}(\frac{1}{N}, \frac{1}{N}, 0)$, where $\theta = \frac{2\pi}{N}$ are the corresponding angles between spins S (assumed to have equal values). This expression has a linear behavior in the low-q limit for spins rotating in the XZ plane,

$$\Delta E_{DMI}^Y(\mathbf{q}) \approx 12S^2 D_y \frac{2\pi}{N}. \quad (2)$$

We use this equation to fit the DFT energies, so that the resulting D_y values are to be interpreted as *effective*, since other contributions, not considered in Eq. (1), also yield linear terms in q for $\hat{s}_a = Y$, such as interplanar nearest neighbor bonds [36], second nearest, and beyond neighbors.

To obtain D_y, we exclude the two largest q values of each curve shown in Fig. 2 and use as spin moment value the average over the Co atomic layers. In the central Co atomic
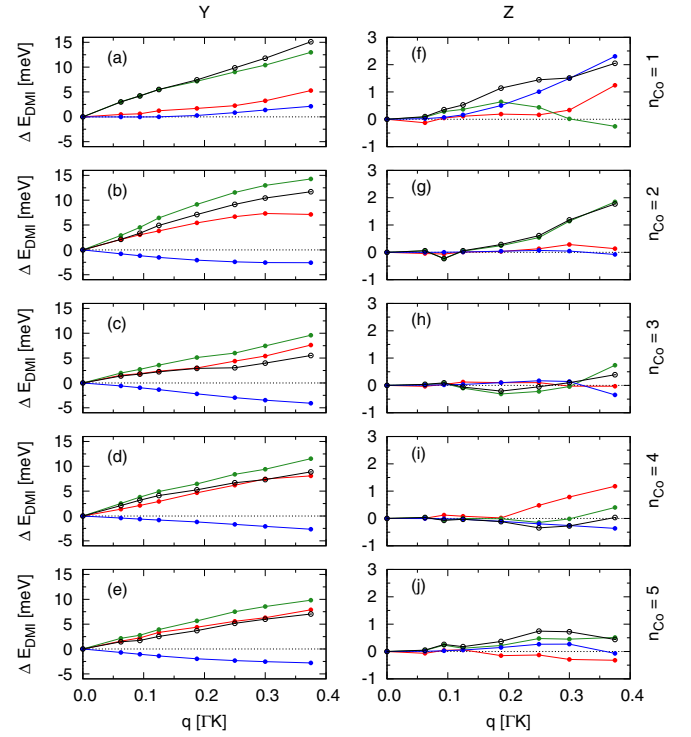

FIG. 2. DMI energy $\Delta E_{DMI}^{\hat{s}_a}(\mathbf{q})$ for spin spirals rotating in the plane perpendicular to Y [panel column (a)–(e)] and Z (f)–(j) axes and Co layer thicknesses (panel rows) in three different heterostructures: $Gr/Co_n/Pt_5$ (red), Co_n/Pt_5 (green), and Gr/Co_n (blue) with $n = 1–5$. In black, the contribution sum from $Co_n/Pt_5 + Gr/Co_n$. The spin spiral wave vector modulus q is given in fractional units of the distance ΓK in the Brillouin zone [see Fig. 1(b)].

planes we find $m_S(Co) \simeq 1.86\mu_B$. This value is slightly enhanced at the vacuum/Co and Co/Pt interfaces ($1.94\mu_B$ for $n_{Co} = 5$), while graphene has a demagnetizing effect ($1.57\mu_B$) (see also the Supplemental Material Fig. S5 middle panels). Additionally, at the interfacial Pt atoms a spin polarization of $0.27\mu_B$ is induced. In the model of Eq. (1), this would add to $\Delta E_{DMI}^Y(\mathbf{q})$ a Co-Pt nearest neighbor contribution one order of magnitude smaller than that of the Co-Co DMI interactions. The resulting D_y values, summarized in Fig. 3, have a very good agreement with linear behavior (the linear fit errors are $\leqslant 4\%$). The D_y values oscillate for $n_{Co} = 1–3$ and converge to $D_y \simeq 0.3$ meV μ_B^{-2} afterwards. The fitted D_y value for Co_1Pt_5 is in agreement with the literature calculated with GBT and flat spin spirals [20,48], too, which are close to 0.5 meV μ_B^{-2}. This methodology tends to yield larger energies than other electronic structure methods [48].

For spins rotating in the interface (XY) plane, the DMI energy is a third order effect in q,

$$\Delta E_{DMI}^Z(\mathbf{q}) \approx -4S^2 D_z \left(\frac{2\pi}{N}\right)^3. \quad (3)$$

This means that at this geometry the interfaces sustain an effective D vector with an out-of-plane component D_z (note that a spin spiral with **q** vector along ΓM would not allow one to resolve D_z), although the magnitude of this effect is small. The second column of Fig. 2 shows that, indeed, the energies are an order of magnitude smaller than for spins rotating in
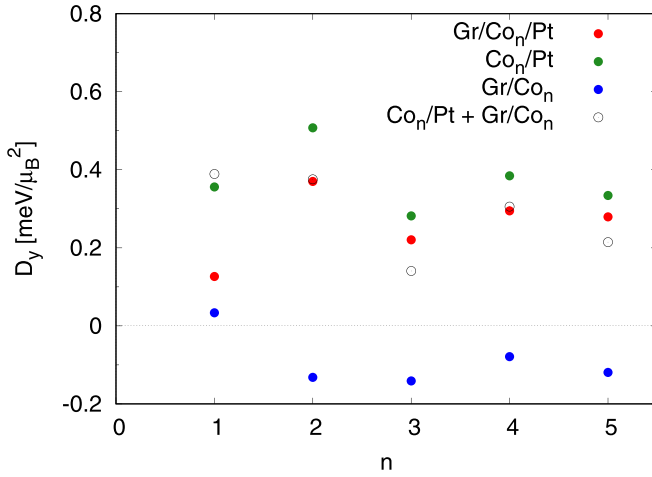
FIG. 3. In-plane components of the effective D vector obtained from fits of the data in the left-hand column of Fig. 2 to a linear law up to $q = 0.25|\Gamma K|$, where the averaged $m_S(\text{Co})$ values over the Co layer have been used.

FIG. 4. Contributions to the DMI energy $\Delta E_{\text{DMI}}^Y(\mathbf{q})$ (spins rotating in the plane perpendicular to Y axis and spiral wave vector along the ΓK reciprocal direction) from the individual interfacial atomic planes in the $\text{Gr}/\text{Co}_5/\text{Pt}_5$ slab and its constituents. The labels indicate the contributing atom and the subindices indicate the interface the atom belongs to, e.g., Co_v is the Co at the vacuum interface.

the XZ plane. These data sets do not allow for a good quality fit to a q^3 law, since the large $\xi(\text{Pt})$ value magnifies finite size effects. Slabs with a single Pt layer as substrate, which are shown in the Supplemental Material Fig. S6, have a smoother behavior. In them $\Delta E_{\text{DMI}}^Z(\mathbf{q})$ changes its sign, i.e., alternating chirality of D_z, as the Co layer grows beyond the monolayer thickness and tends toward small values when interfaces are decoupled at $n_{\text{Co}} = 3$. A sizable nonzero D_z component can result in hybrid Bloch-Néel domain walls [49] and it has been postulated that it is responsible for an asymmetric skyrmion Hall effect [50]. In addition, the effect of the nearest-neighbor interplanar interaction energy term for $n_{\text{Co}} = 2$ is clearly distinguished in the $\Delta E_{\text{DMI}}^Y(\mathbf{q})$ curve (see Fig. S6).

In the remainder of the paper we focus the analysis on the D_y component only. To ascertain whether the crossover at $n_{\text{Co}} = 3$ is correlated with the additivity of interfacial DMI, we have decomposed the heterostructure model slab into $\text{Co}_{1-5}/\text{Pt}_5$ and $\text{Gr}/\text{Co}_{1-5}$ partial slabs with the same atomic positions (green and blue lines and symbols, respectively, in Fig. 2 and Fig. 3). In the following, we call this form of analysis "partial slab decomposition" (PSD). The sum of the corresponding $\Delta E_{\text{DMI}}^Y(\mathbf{q})$ and effective D_y (black lines and open symbols) follows closely the $\text{Gr}/\text{Co}_{2-5}/\text{Pt}_5$ values, while there is a large difference for $n_{\text{Co}} = 1$. Although this would suggest that the Co/Pt and Gr/Co interfaces are already decoupled at $n_{\text{Co}} = 2$, their individual values still depend on the Co thickness. Hence effective decoupling does not occur until at least $n_{\text{Co}} = 3$. In particular, for $\text{Gr}/\text{Co}_2/\text{Pt}_5$ the maximum value $D_y = 0.5$ meV μ_B^{-2} is obtained.

The contribution of the Co/Pt interface accounts for most of the $\Delta E_{\text{DMI}}^Y(\mathbf{q})$ energy in the heterostructure. Importantly, at the Gr/Co interface the chirality is opposite (except in the GrCo bilayer) and of comparable magnitude to that of Co/Pt. This type of analysis, however, cannot determine if the effect of the Gr capping layer is to invert the chirality of the vacuum/Co interface. For this, we have calculated $\Delta E_{\text{DMI}}^Y(\mathbf{q})$ with atomic SOC contributions selected in the respective atomic spheres [47], a method we denote in the following with
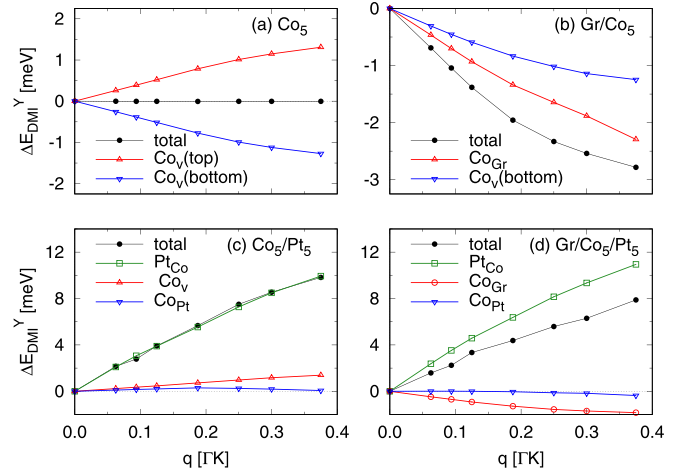
the acronym ASOD (atomic spin-orbit decomposition). These results are shown in Fig. 4. This alternative method allows one to assess the individual atom contributions to interfacial DMI energy in a given system, since it is additive in the atomic SOC strength (ξ) by construction. With ASOD we find that the contribution of the interfacial Pt atomic plane, Pt_{Co}, dominates the whole DMI effect, showing similar energies in both $\text{Gr}/\text{Co}_5/\text{Pt}_5$ and Co_5/Pt_5 slabs, whereas the Co plane in that same interface, Co_{Pt}, has a negligible contribution compared to Co_{Gr}, as also reported in the literature for similar $3d/5d$ interfaces [19,20]. This is explained in part by the strength of SOC at Pt, which is one order of magnitude larger than at Co ($\xi_{\text{Co}} = 76$ meV and $\xi_{\text{Pt}} = 618$ meV, given by the present FLAPW calculations). In the case of a bare Co_5 slab, the two outermost atomic planes contribute with opposite chiralities and sizable values, namely $|D_y| = 0.175$ meV μ_B^{-2}. Importantly, we find that the Co contribution changes from positive to negative D_y and it is nearly doubled in magnitude when it is in contact with graphene in the Gr/Co_5 slab (the contribution of graphene itself is negligible due to the small ξ_C value). Therefore, graphene has the effect of reducing the net DMI of $\text{Gr}/\text{Co}_n(\text{fcc}^\star)/\text{Pt}$ heterostructures by inducing in the topmost Co plane an opposite chirality to that of the Co/Pt interface. This has been observed by MOKE microscopy in domain wall propagation experiments, although the graphene effect on the DMI was reported there to be about one-half of that of the Co/Pt interface (the reported spatial micromagnetic averages are 1.4 and -0.8 mJ/m^2 for the Co/Pt [12] and Gr/Co [26] interfaces).

We have used two methods for the resolution of the DMI energy into its individual interfacial terms. The PSD method accounts for the joint effect of (i) the SOC strength and (ii) the electronic structure modification at the interface when the constituents are brought together. In the ASOD method *only the relativistic effect is being probed*. The latter method is less realistic, but more informative. The importance of effect

TABLE I. Electric dipole (atomic units) in the direction perpendicular to the interfaces inside the FLAPW muffin-tin spheres (p_z) for the interfacial atoms in the Gr/Co$_n$/Pt$_5$, Co$_n$/Pt$_5$, and Gr/Co$_n$ slabs with $n = 1, 5$. The subindex in the first column indicates the neighboring atomic layer in the interface. At graphene, the p_z of the two sublattice C atoms is averaged.

Atom	Gr/Co$_1$/Pt$_5$	Co$_1$/Pt$_5$	Gr/Co$_1$
C	0.014		0.014
Co	−0.111	0.153	−0.267
Pt$_{Co}$	−0.092	−0.088	
Atom	Gr/Co$_5$/Pt$_5$	Co$_5$/Pt$_5$	Gr/Co$_5$
C	0.013		0.013
Co$_{Gr}$ (Co$_v$)	−0.043	(0.197)	−0.043
Co$_{Pt}$ (Co$_v$)	−0.059	−0.060	(−0.195)
Pt$_{Co}$	−0.077	−0.077	

(ii) is manifested in the DMI tuning by adsorption of light atoms. For example, H adsorption on Ni/Co/Pd/W induces chirality change [22], with the advantage that H uptake and desorption is a reversible process [22,23]. DMI changes have also been characterized during oxidation of $3d/5d$ layered systems [24,25]. This DMI behavior is associated to a charge density redistribution upon adsorption and, based on this mechanism, electrostatic properties such as surface dipoles, work functions, and electronegativity have been proposed as DMI descriptors [24,28].

Table I shows the perpendicular electric dipole p_z of the interfacial C, Co, and Pt atoms of the three partial slabs in the limit cases $n_{Co} = 1$ and 5. It is evaluated as $p_z = -|e|\langle z \rangle_{MT}$, where the average position is evaluated as an integral over the charge density distribution inside the muffin tin. For the interfaces at the top of the slab, $p_z > 0$ ($p_z < 0$) means that the dipole points outward (inward) and vice versa for the interfaces at the slab bottom. For $n_{Co} = 1$, p_z(Co) depends strongly on the interface type: the dipole points inward when coated with graphene and outward when not. At the top of the $n_{Co} = 5$ slab a sign inversion of p_z due to graphene is observed, too, alongside a reduction of the p_z magnitude from 0.197 to 0.043 a.u. (a factor 4.6). At the buried Co/Pt interface, Pt has also the effect of reducing the dipole of the interfacial Co$_{Pt}$ atom by a factor 3.25 with respect to Co$_v$, but no sign inversion occurs. As reported in Ref. [28], the p_z are correlated with DMI energies. In the present case of the slabs with $n_{Co} = 5$, there is agreement between the signs of the p_z of interfacial Co atoms (Table I) and the signs of the contributions of these atoms to ΔE_{DMI}^Y (Fig. 4). However, there is no proportionality between the two magnitudes. Note that dipoles and electronegativity are related to the D vector by a nonlinear analytical expression, which results in an approximately linear correlation between these properties for different adsorbed species [28].

We investigate next the influence of the Co stacking on the DMI, known to be a key factor to explain the magnetocrystalline anisotropy of Gr/Co/Pt heterostructures. When Co is pseudomorphically grown by intercalation in Gr/Pt(111), it results in a fcc* stacking rather than hcp [26,51], with stacking defects scattered throughout, nucleating predomi-

nantly near the Pt(111) substrate steps [35]. In a perfect fcc* heterostructure, DFT calculations show that the magnetocrystalline anisotropy energy (MAE) follows a bulklike behavior with in-plane anisotropy starting at $n_{Co} = 8$ (0.09 meV per Co atom, imposed by the lateral fcc* lattice strain) and the critical thickness for perpendicular to in-plane switching at $n_{Co}^c = 4$. However, the experimental switch occurs later, at $n_{Co}^c \simeq 20$ (about 4 nm), due to defects. The theory shows that each twin boundary contributes with nearly 1 meV to out-of-plane anisotropy, as it introduces locally a hcp stacked structure [35].

Figure 5 shows atom-resolved $\Delta E_{DMI}^Y(\mathbf{q})$ for Gr/Co$_5$/Pt$_5$ with Co in three different stackings [panels (a)–(c)]: Perfect hcp, fcc* stacking with a twin boundary defect at the middle Co plane, labeled tb3 in the following, and perfect fcc*. As in the original fcc* heterostructure, with the hcp and tb3 stackings the large ξ_{Pt} dominates the net DMI, contributing similar energies (black symbols). In the case of a perfect fcc* growth, the central region of the Co layer is locally almost centrosymmetric and therefore will not contribute to DMI. Nevertheless, in this finite-thickness model, we observe that the Co atomic plane contributions oscillate around zero. Oscillating values occur for the tb3 and the hcp slabs, with larger energies in the latter. Note that for bare Co$_5$ slabs with the same geometries, i.e., in the absence of interfaces with Gr and Pt, cancellations at the Co planes are almost total irrespective of the stacking type [red symbols in Fig. 5(d)]. There is an overall negative contribution of the Co planes to the DMI [black symbols in Fig. 5(d)] that has its main origin at the Gr/Co interface. Sizable DMI occurs at the Gr/Co and Co/Pt interfaces, while buried interfaces in Co that break inversion symmetry locally contribute almost negligibly. This behavior contrasts with that of the magnetic anisotropy, despite both properties sharing a common origin in the SOC, with MAE being of ξ^2 order at this symmetry and DMI being linear in ξ. Therefore, in the Gr/Co/Pt heterostructure DMI and magnetocrystalline anisotropy are at play on an equal footing only close to the critical thicknesses, when the fcc* bulk limit and the defect contributions compensate each other to give a low MAE. The effect of the strained Co lattice constant on the Gr/Co interfacial DMI contribution is negligible, as long as the Gr-Co interplanar distances are similar, which ensures a similar hybridization [52–55]. This has been checked in a calculation for the Gr/Co$_5$ slab with the experimental hcp Co lattice constant (see Supplemental Material Fig. S7).

B. Reciprocal space analysis

So far, in the literature, interfacial DMI has been discussed in terms of two different mechanisms: A Rashba-like behavior in Gr/Co triggered by the surface potential change ∇V induced by graphene adsorption [31] or, alternatively, a Fert-Levy-like behavior in Co/Pt, where Pt SOC mediates the spin flip of the Co itinerant electrons. The aim of this section is to identify the nature of DMI at those interfaces based on information gathered at the reciprocal space. The explicit dependence of DMI on each Bloch eigenstate $\epsilon_{nk}(\mathbf{q})$ is too intricate to be analyzed by a bare eye, due to the high density of dispersive bands in the Gr/Co$_n$/Pt$_5$ models (see Supplemental Material Fig. S8). Note that each band is subject
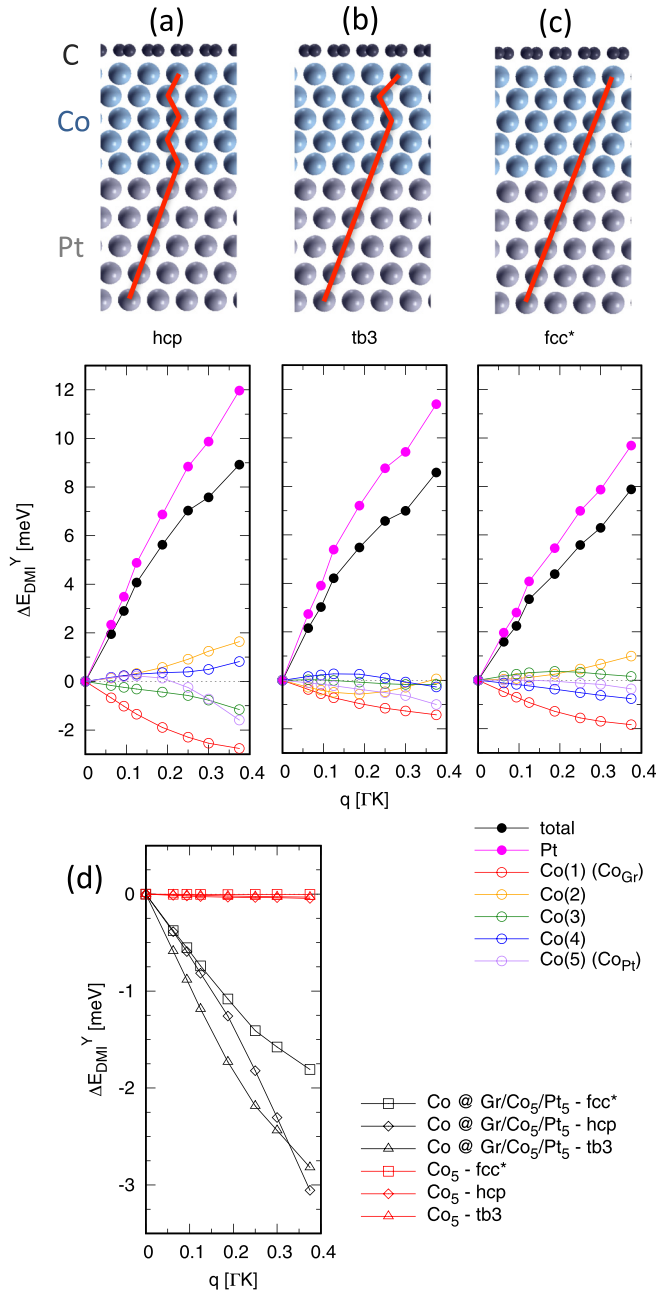
FIG. 5. (a)–(c) Top panels: cross section of the $Gr/Co_5/Pt_5$ slabs with different Co stacking geometries: Perfect hcp, fcc★ with a twin boundary introduced in the middle Co plane (tb3) and perfect fcc★. A red line indicates the stacking sequences. Bottom panels: For each geometry, total DMI energies $[\Delta E_{DMI}^Y(q)]$ for spins rotating in the plane perpendicular to Y (black filled circles) and those obtained when SOC is applied only to the indicated atomic planes (colored filled circles for Pt layer and empty for individual atomic planes). (d) Co layer contributions from $Gr/Co_5/Pt_5$ slabs (black symbols) compared to bare Co_5 slabs with the three stacking types (red symbols).

to lateral shifts due to the spin spirals and to degeneracy liftings, mainly at crossings between bands, due to SOC (see Supplemental Material Fig. S8), as shown by Sandratskii for
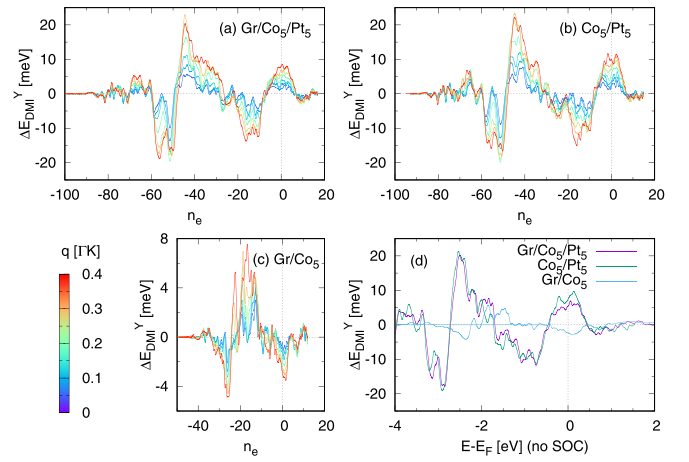

FIG. 6. (a)–(c) DMI energy $[\Delta E_{DMI}^Y(q)]$ as a function of the band filling for the $Gr/Co_5/Pt_5$, Co_5/Pt_5, and Gr/Co_5 slabs. The color scale bar indicates the q magnitude on a scale from 0 (Γ) to 1 (K). (d) The same curves plotted as a function of energy (referred to the Fermi levels of each slab calculated without SOC) for the particular point $q = 0.25|\Gamma K|$.

the CoPt bilayer [21]. Instead, in our analysis we use quantities integrated in energies and in electron wave vectors **k**.

To analyze the spectral behavior of the DMI chirality, we plot the corresponding energies integrated in **k** as a function of the number of electrons n_e for each spin spiral vector **q**. This is similar to the MAEs in the force theorem approach [56,57]:

$$\Delta E_{DMI}^Y(n_e; \mathbf{q}) = \sum_{nk} \epsilon_{nk}^{Y^+}(\mathbf{q}) f\left(\epsilon_{nk}^{Y^+}(\mathbf{q}) - \epsilon_F^{Y^+}(n_e; \mathbf{q})\right)$$
$$- \epsilon_{nk}^{Y^-}(\mathbf{q}) f\left(\epsilon_{nk}^{Y^-}(\mathbf{q}) - \epsilon_F^{Y^-}(n_e; \mathbf{q})\right), \quad (4)$$

where **q** is a spin spiral wave vector along ΓK, the sum runs over the eigenvalues ϵ_{nk} calculated for opposite spin rotation axes (Y^+ and Y^-), and the Fermi levels correspond to the filling up with n_e electrons of the bands of each individual calculation with **q** and Y^+ or Y^-. The $\Delta E_{DMI}^Y(n_e; \mathbf{q})$ curves for $Gr/Co_5/Pt_5$, Co_5/Pt_5, and Gr/Co_5 slabs are qualitatively stable with q (see Fig. 6): The nodes in the curves are almost invariant and peaks only increase in amplitude with q, resulting in the linear dependence observed in the previous section. This behavior occurs also in the less complex CoPt bilayer, where it has been explained [21] by the hybridization of the spiral electron states with wave vectors **k** and $\mathbf{k} \pm \mathbf{q}$, which have similar character regardless of **q**, giving rise to the dependence of Eq. (1) [58]. As observed in Fig. 6, this scenario is not affected by the presence of the large number of additional bands of a thicker Pt substrate, which is the reciprocal space confirmation that the DMI is localized within a very short spatial range (bond length distance) of the interface. At neutrality ($n_e = 0$) the known positive $\Delta E_{DMI}^Y(0; \mathbf{q})$ values for $Gr/Co_5/Pt_5$ and Co_5/Pt_5 and negative for Gr/Co_5 are retrieved. The sign of the DMI energy is kept under small variations of n_e around the neutrality condition. When represented as a function of binding energies, $\Delta E_{DMI}^Y(n_e; \mathbf{q})$ has the last node before neutrality at the filling corresponding to $E_F - 0.5$ eV in the three slabs, as shown in the Fig. 6(d) panel for $\mathbf{q} = \frac{2\pi}{a}(\frac{1}{12}, \frac{1}{12}, 0)$. This means that integration of eigenen-
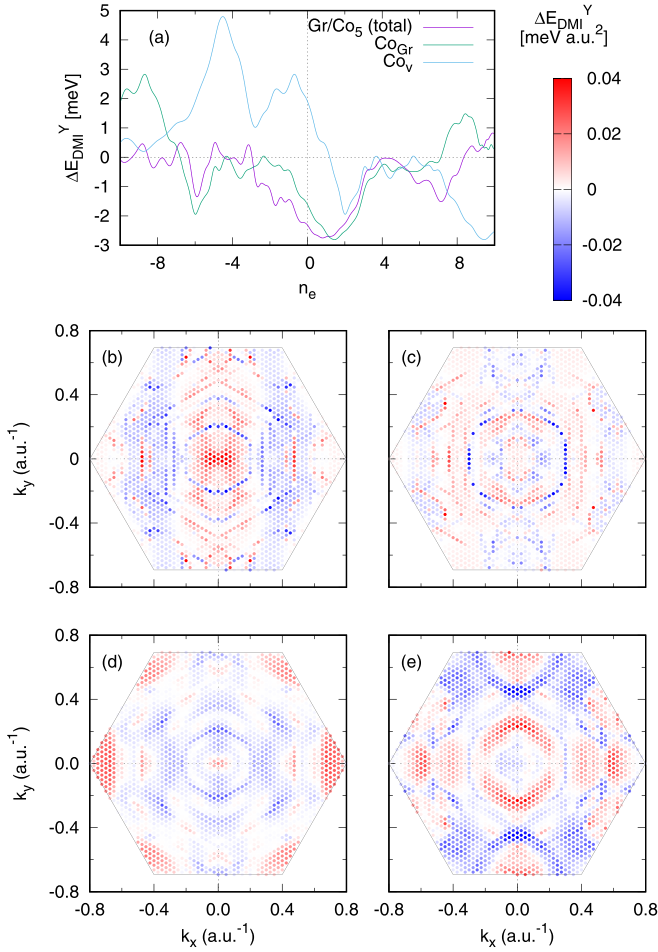
FIG. 7. (a) $\Delta E_{DMI}(n_e)$ at $q = 0.25|\Gamma K|$ for the Gr/Co$_5$ slab (purple) compared with the curves calculated for SOC applied only to the Co$_{Gr}$ plane of that slab (green) and to Co$_v$ of the clean Co$_5$ slab (blue) (note that the latter is centrosymmetric; thus the total ΔE_{DMI}^Y in the slab amounts to zero). (b)–(e) For the same **q** vector, ΔE_{DMI}^Y at $n_e = 0$ resolved in k space. Panels (b), (d) correspond to the Co$_{Gr}$ interfacial atomic plane and (c), (e) to Co$_v$ (Co/vacuum interface). Data of panels (b), (c) are calculated by integration over all the occupied bands. In panels (d), (e), the integral energy range is restricted to a stripe of 0.5 eV below the Fermi level. Note that the modified basis used for the GBT breaks the hexagonal symmetry [42,43].

ergies in this energy window of 0.5 eV would *effectively* reproduce the net DMI, albeit nonzero DMI contributions occur throughout the whole available energy spectrum. This is evident with a Pt substrate, since the $5d - 3d$ hybrid bandwidth spans several eV. However, Figs. 6(c) and 6(d) show the same qualitative behavior for Gr/Co$_5$, pointing out that there is a similar DMI mechanism here due only to the Co SOC contributions. Note that the 0.5 eV window coincidence for the three slabs is fortuitous, as it depends on the particular details of each band structure.

With focus on the DMI chirality inversion of the vacuum/Co interface upon capping with graphene, we first verify that the $\Delta E_{DMI}(0;\mathbf{q})$ values reproduce the sign change when evaluated with only the corresponding interfacial individual atomic SOC strength ξ_{Co} [see Fig. 7(a)]. We now turn to a **k**-resolved analysis of these quantities. Figures 7(b) and

7(c) show that DMI is not localized in the **k** space, but broad regions of the Brillouin zone (BZ) contribute with opposite chiralities to the final net $\Delta E_{DMI}(0;\mathbf{q})$ in both vacuum/Co and Gr/Co interfaces. Owing to the found effective energy window, in Figs. 7(d) and 7(e) we restrict the **k**-resolved analysis to an integral over states within a window of 0.5 eV below the Fermi level. We observe that the Co-C hybrid bands, with nearly conical dispersion at the K, K' special points, yield a positive contribution to $\Delta E_{DMI}(0;\mathbf{q})$ (red spots at the BZ vertices), whereas the rest of the BZ contributes with negative values. In other words, the distinctive feature of the graphene adsorption on the band structure, namely the conical band of C-p_z and Co-d_{z^2} character, as well as a small weight in $d_{xz,yz}$ orbitals, actually contributes to a chirality opposite to the observed one. The conclusion is that the DMI of the Gr/Co interface cannot be attributed to individual Co-C hybrid bands near the Fermi level. For this reason, a model where the D vector is estimated from a Rashba Hamiltonian $\alpha_R(\boldsymbol{\sigma} \times \mathbf{k})_z$ of a single band in a ferromagnetically coupled environment [27,31,33,34] is not suitable for the Gr/Co interface. In particular, the expression $D = 4\alpha_R m^\star A/\hbar^2$, where A is the exchange stiffness [33], is no longer valid beyond the Rashba approximation [59]. Instead, the contributing Co-C interactions extend to the whole spectrum. On this basis we can state that the interfacial DMI at Gr/Co and Co/Pt has similar contribution from the strongly hybridized SOC-split d bands. We recall that Rashba band splitting requires not only a ∇V, which can be indeed enhanced upon adsorption if this increases the asymmetry of the charge distribution at the surface [60], but also a substantial SOC strength ξ [61,62].

IV. CONCLUSIONS

Our interface-resolved DFT study of DMI in Gr/Co$_n$/Pt(111) heterostructures with varying Co layer thickness shows that the regime of additivity of interfacial DMI is reached already at $n = 3$ atomic planes and also that the D vectors have an almost negligible out-of-plane component. As the perpendicular magnetocrystalline anisotropy prevails up to much larger n values [35], a sizable DMI interaction to have spin canting and chiral exchange effects are expected to be robust with the film thickness. However, unlike the magnetocrystalline anisotropy itself, interfacial DMI is insensitive to the internal structure of the Co layer. The observed DMI in domain wall propagation suggests a comparable interface DMI strength but opposite sign at Gr/Co and Co/Pt interfaces [35]. This is confirmed by our calculations. Indeed, we find that the graphene layer has the effect of inverting the chirality of the vacuum/Co interface.

The Gr/Co and Co/Pt interfacial DMI has been classified as being of different nature, namely, Rashba and Fert-Levy mechanisms at Gr/Co and Co/Pt, respectively. Our study leads to the conclusion that this classification is subjective. Those models correspond to two limiting cases of the same physics, as illustrated by the Gr/Co$_n$/Pt system. The electrostatic dipole (a magnitude identified as a DMI descriptor) at the vacuum/Co surface is reversed and increases in magnitude upon capping with graphene. Nevertheless, this does not mean that the effects can be explained by an overall Rashba

term acting on all bands with the same strength and sign. Instead, the superposition of many hybridized bands with weight on the Co atoms can contribute to the interfacial DMI at both Gr/Co and Co/Pt. A band-dependent and generalized (nonlinear in k) Rashba model is probably more appropriate for the accurate description of DMI at the Co/Gr interface. In other heterostructures with $2p/3d/5d$ composition, where nontrivial hybridization of the $3d$ bands with the ones of the $5d$ substrate and the $2p$ orbitals is foreseen, the DMI should be analyzed in the same way. This means that all bands must be treated on an equal footing and with no approximations on the functional form of the SOC terms.

[1] I. E. Dzialoshinskii, Sov. Phys. JETP **5**, 1259 (1957).

[2] T. Moriya, Phys. Rev. Lett. **4**, 228 (1960).

[3] T. Moriya, Phys. Rev. **120**, 91 (1960).

[4] A. Fert and P. M. Levy, Phys. Rev. Lett. **44**, 1538 (1980).

[5] P. M. Levy and A. Fert, Phys. Rev. B **23**, 4667 (1981).

[6] M. Bode, M. Heide, K. von Bergmann, P. Ferriani, S. Heinze, G. Bihlmayer, A. Kubetzka, O. Pietzsch, S. Blügel, and R. Wiesendanger, Nature (London) **447**, 190 (2007).

[7] M. Schmitt, P. Moras, G. Bihlmayer, R. Cotsakis, M. Vogt, J. Kemmer, A. Belabbes, P. M. Sheverdyaeva, A. K. Kundu, C. Carbone, S. Blügel, and M. Bode, Nat. Commun. **10**, 2610 (2019).

[8] R. Wiesendanger, Nat. Rev. Mater. **1**, 16044 (2016).

[9] A. Fert, N. Reyren, and V. Cros, Nat. Rev. Mater. **2**, 17031 (2017).

[10] A. N. Bogdanov and C. Panagopoulos, Nat. Rev. Phys. **2**, 492 (2020).

[11] M. Heide, G. Bihlmayer, and S. Blügel, Phys. Rev. B **78**, 140403(R) (2008).

[12] Z. Luo, T. P. Dao, A. Hrabec, J. Vijayakumar, A. Kleibert, M. Baumgartner, E. Kirk, J. Cui, T. Savchenko, G. Krishnaswamy, L. J. Heyderman, and P. Gambardella, Science **363**, 1435 (2019).

[13] A. Hrabec, Z. Luo, L. J. Heyderman, and P. Gambardella, Appl. Phys. Lett. **117**, 130503 (2020).

[14] E. Y. Vedmedenko, R. K. Kawakami, D. D. Sheka, P. Gambardella, A. Kirilyuk, A. Hirohata, C. Binek, O. Chubykalo-Fesenko, S. Sanvito, B. J. Kirby, J. Grollier, K. Everschor-Sitte, T. Kampfrath, C.-Y. You, and A. Berger, J. Phys. D **53**, 453001 (2020).

[15] C. Moreau-Luchaire, C. Moutafis, N. Reyren, J. Sampaio, C. A. F. Vaz, N. Van Horne, K. Bouzehouane, K. Garcia, C. Deranlot, P. Warnicke, P. Wohlhüter, J.-M. George, M. Weigand, J. Raabe, V. Cros, and A. Fert, Nat. Nanotechnol. **11**, 444 (2016).

[16] H. Yang, O. Boulle, V. Cros, A. Fert, and M. Chshiev, Sci. Rep. **8**, 12356 (2018).

[17] M. Perini, S. Meyer, B. Dupé, S. von Malottki, A. Kubetzka, K. von Bergmann, R. Wiesendanger, and S. Heinze, Phys. Rev. B **97**, 184425 (2018).

[18] S. Woo, K. Litzius, B. Krüger, M.-Y. Im, L. Caretta, K. Richter, M. Mann, A. Krone, R. M. Reeve, M. Weigand, P. Agrawal, I. Lemesh, M.-A. Mawass, P. Fischer, M. Kläui, and G. S. D. Beach, Nat. Mater. **15**, 501 (2016).

[19] H. Yang, A. Thiaville, S. Rohart, A. Fert, and M. Chshiev, Phys. Rev. Lett. **115**, 267210 (2015).

[20] A. Belabbes, G. Bihlmayer, F. Bechstedt, S. Blügel, and A. Manchon, Phys. Rev. Lett. **117**, 247202 (2016).

[21] L. M. Sandratskii, Phys. Rev. B **96**, 024450 (2017).

[22] G. Chen, M. C. Robertson, M. Hoffmann, C. Ophus, A. L. Fernandes Cauduro, R. Lo Conte, H. Ding, R. Wiesendanger, S. Blügel, A. K. Schmid, and K. Liu, Phys. Rev. X **11**, 021015 (2021).

[23] B. Yang, Q. Cui, J. Liang, M. Chshiev, and H. Yang, Phys. Rev. B **101**, 014406 (2020).

[24] A. Belabbes, G. Bihlmayer, S. Blügel, and A. Manchon, Sci. Rep. **6**, 24634 (2016).

[25] G. Chen, A. Mascaraque, H. Jia, B. Zimmermann, M. Robertson, R. L. Conte, M. Hoffmann, M. A. González Barrio, H. Ding, R. Wiesendanger, E. G. Michel, S. Blügel, A. K. Schmid, and K. Liu, Sci. Adv. **6**, eaba4924 (2020).

[26] F. Ajejas, A. Gudín, R. Guerrero, A. Anadón Barcelona, J. M. Diez, L. de Melo Costa, P. Olleros, M. A. Niño, S. Pizzini, J. Vogel, M. Valvidares, P. Gargiani, M. Cabero, M. Varela, J. Camarero, R. Miranda, and P. Perna, Nano Lett. **18**, 5364 (2018).

[27] A. Hallal, J. Liang, F. Ibrahim, H. Yang, A. Fert, and M. Chshiev, Nano Lett. **21**, 7138 (2021).

[28] H. Jia, B. Zimmermann, G. Michalicek, G. Bihlmayer, and S. Blügel, Phys. Rev. Materials **4**, 024405 (2020).

[29] S. Kim, K. Ueda, G. Go, P.-H. Jang, K.-J. Lee, A. Belabbes, A. Manchon, M. Suzuki, Y. Kotani, T. Nakamura, K. Nakamura, T. Koyama, D. Chiba, K. T. Yamada, D.-H. Kim, T. Moriyama, K.-J. Kim, and T. Ono, Nat. Commun. **9**, 1648 (2018).

[30] P.-J. Hsu, A. Kubetzka, A. Finco, N. Romming, K. von Bergmann, and R. Wiesendanger, Nat. Nanotechnol. **12**, 123 (2017).

[31] H. Yang, G. Chen, A. A. C. Cotta, A. T. N'Diaye, S. A. Nikolaev, E. A. Soares, W. A. A. Macedo, K. Liu, A. K. Schmid, A. Fert, and M. Chshiev, Nat. Mater. **17**, 605 (2018).

[32] H. Imamura, P. Bruno, and Y. Utsumi, Phys. Rev. B **69**, 121303(R) (2004).

[33] K.-W. Kim, H.-W. Lee, K.-J. Lee, and M. D. Stiles, Phys. Rev. Lett. **111**, 216601 (2013).

[34] A. Kundu and S. Zhang, Phys. Rev. B **92**, 094434 (2015).

[35] M. Blanco-Rey, P. Perna, A. Gudin, J. M. Diez, A. Anadon, P. Olleros-Rodriguez, L. de Melo Costa, M. Valvidares, P. Gargiani, A. Guedeja-Marron, M. Cabero, M. Varela, C. Garcia-Fernandez, M. M. Otrokov, J. Camarero, R. Miranda, A. Arnau, and J. I. Cerda, ACS Appl. Nano Mater. **4**, 4398 (2021).

[36] A. Crépieux and C. Lacroix, J. Magn. Magn. Mater. **182**, 341 (1998).

[37] See Supplemental Material at http://link.aps.org/supplemental/10.1103/PhysRevB.106.064426 for further calculation details, dependence on thickness and lattice constant, and band structures.

[38] S. Meyer, M. Perini, S. von Malottki, A. Kubetzka, R. Wiesendanger, K. von Bergmann, and S. Heinze, Nat. Commun. **10**, 3823 (2019).

[39] P. Olleros-Rodríguez, R. Guerrero, J. Camarero, O. Chubykalo-Fesenko, and P. Perna, ACS Appl. Mater. Interfaces **12**, 25419 (2020).

[40] H. Krakauer, M. Posternak, and A. J. Freeman, Phys. Rev. B **19**, 1706 (1979).

[41] E. Wimmer, H. Krakauer, M. Weinert, and A. J. Freeman, Phys. Rev. B **24**, 864 (1981).

[42] FLEUR site: http://www.flapw.de.

[43] P. Kurz, F. Förster, L. Nordström, G. Bihlmayer, and S. Blügel, Phys. Rev. B **69**, 024415 (2004).

[44] J. P. Perdew, K. Burke, and M. Ernzerhof, Phys. Rev. Lett. **77**, 3865 (1996).

[45] H. J. Monkhorst and J. D. Pack, Phys. Rev. B **13**, 5188 (1976).

[46] L. M. Sandratskii, J. Phys.: Condens. Matter **3**, 8565 (1991).

[47] M. Heide, G. Bihlmayer, and S. Blügel, Phys. B: Condens. Matter **404**, 2678 (2009).

[48] B. Zimmermann, G. Bihlmayer, M. Böttcher, M. Bouhassoune, S. Lounis, J. Sinova, S. Heinze, S. Blügel, and B. Dupé, Phys. Rev. B **99**, 214426 (2019).

[49] D. Lee, R. K. Behera, P. Wu, H. Xu, Y. L. Li, S. B. Sinnott, S. R. Phillpot, L. Q. Chen, and V. Gopalan, Phys. Rev. B **80**, 060102(R) (2009).

[50] K.-W. Kim, K.-W. Moon, N. Kerber, J. Nothhelfer, and K. Everschor-Sitte, Phys. Rev. B **97**, 224427 (2018).

[51] F. Ajejas, A. Anadon, A. Gudin, J. M. Diez, C. G. Ayani, P. Olleros-Rodríguez, L. de Melo Costa, C. Navío, A. Gutiérrez, F. Calleja, A. L. Vázquez de Parga, R. Miranda, J. Camarero, and P. Perna, ACS Appl. Mater. Interfaces **12**, 4088 (2020).

[52] A. Varykhalov, D. Marchenko, M. R. Scholz, E. D. L. Rienks, T. K. Kim, G. Bihlmayer, J. Sánchez-Barriga, and O. Rader, Phys. Rev. Lett. **108**, 066804 (2012).

[53] D. Marchenko, A. Varykhalov, J. Sánchez-Barriga, O. Rader, C. Carbone, and G. Bihlmayer, Phys. Rev. B **91**, 235431 (2015).

[54] D. Usachov, A. Fedorov, M. M. Otrokov, A. Chikina, O. Vilkov, A. Petukhov, A. G. Rybkin, Y. M. Koroteev, E. V. Chulkov, V. K. Adamchuk, A. Grüneis, C. Laubschat, and D. V. Vyalikh, Nano Lett. **15**, 2396 (2015).

[55] M. M. Otrokov, I. I. Klimovskikh, F. Calleja, A. M. Shikin, O. Vilkov, A. G. Rybkin, D. Estyunin, S. Muff, J. H. Dil, A. L. V. de Parga, R. Miranda, H. Ochoa, F. Guinea, J. I. Cerdá, E. V. Chulkov, and A. Arnau, 2D Mater. **5**, 035029 (2018).

[56] G. H. O. Daalderop, P. J. Kelly, and M. F. H. Schuurmans, Phys. Rev. B **50**, 9989 (1994).

[57] M. Blanco-Rey, J. I. Cerdá, and A. Arnau, New J. Phys. **21**, 073054 (2019).

[58] Some selection rules are found concerning the orbital character $|l, m\rangle$ of the states with wave vectors $\mathbf{k}$ and $\mathbf{k} \pm \mathbf{q}$. When the $\mathbf{q}$ dependence is perturbatively considered in the analytical D-vector expression, a dipolar term appears that couples different l channels, as shown in Ref. [28]. If only the inversion symmetry breaking is considered, as in Ref. [23], only the couplings between $|2, m\rangle$ orbitals of suitable symmetry (determined by the SOC term in the Hamiltonian [63]) survive.

[59] I. A. Ado, A. Qaiumzadeh, R. A. Duine, A. Brataas, and M. Titov, Phys. Rev. Lett. **121**, 086802 (2018).

[60] O. Krupin, G. Bihlmayer, K. Starke, S. Gorovikov, J. E. Prieto, K. Döbrich, S. Blügel, and G. Kaindl, Phys. Rev. B **71**, 201403(R) (2005).

[61] S. LaShell, B. A. McDougall, and E. Jensen, Phys. Rev. Lett. **77**, 3419 (1996).

[62] L. Petersen and P. Hedegård, Surf. Sci. **459**, 49 (2000).

[63] E. Abate and M. Asdente, Phys. Rev. **140**, A1303 (1965).